Simulation of self-generated magnetic fields in an inertial fusion hohlraum environment

W. A. Farmer, J. M. Koning, D. J. Strozzi, D. E. Hinkel, L. F. Berzak Hopkins, O. S. Jones, and M. D. Rosen

Citation: Physics of Plasmas **24**, 052703 (2017); doi: 10.1063/1.4983140
View online: http://dx.doi.org/10.1063/1.4983140
View Table of Contents: http://aip.scitation.org/toc/php/24/5
Published by the American Institute of Physics

Simulation of self-generated magnetic fields in an inertial fusion hohlraum environment

W. A. Farmer, J. M. Koning, D. J. Strozzi, D. E. Hinkel, L. F. Berzak Hopkins, O. S. Jones, and M. D. Rosen
Lawrence Livermore National Laboratory, 7000 East Ave., Livermore, California 94550, USA

(Received 21 February 2017; accepted 25 April 2017; published online 9 May 2017)

We present radiation-hydrodynamic simulations of self-generated magnetic field in a hohlraum, which show an increased temperature in large regions of the underdense fill. Non-parallel gradients in electron density and temperature in a laser-heated plasma give rise to a self-generated field by the "Biermann battery" mechanism. Here, HYDRA simulations of three hohlraum designs on the National Ignition Facility are reported, which use a partial magnetohydrodynamic (MHD) description that includes the self-generated source term, resistive dissipation, and advection of the field due to both the plasma flow and the Nernst term. Anisotropic electron heat conduction parallel and perpendicular to the field is included, but not the Righi-Leduc heat flux. The field strength is too small to compete significantly with plasma pressure, but affects plasma conditions by reducing electron heat conduction perpendicular to the field. Significant reductions in heat flux can occur, especially for high Z plasma, at modest values of the Hall parameter, $\Omega_e\tau_{ei}\lesssim 1$, where $\Omega_e = eB/m_ec$ and τ_{ei} is the electron-ion collision time. The inclusion of MHD in the simulations leads to 1 keV hotter electron temperatures in the laser entrance hole and high-Z wall blowoff, which reduces inverse-bremsstrahlung absorption of the laser beam. This improves propagation of the inner beams pointed at the hohlraum equator, resulting in a symmetry shift of the resulting capsule implosion towards a more prolate shape. The time of peak x-ray production in the capsule shifts later by only 70 ps (within experimental uncertainty), but a decomposition of the hotspot shape into Legendre moments indicates a shift of P_2/P_0 by $\sim$20%. This indicates that MHD cannot explain why simulated x-ray drive exceeds measured levels, but may be partially responsible for failures to correctly model the symmetry. *Published by AIP Publishing.*
[http://dx.doi.org/10.1063/1.4983140]

I. INTRODUCTION

In the pursuit of inertial confinement fusion (ICF), the indirect drive concept involves illuminating a radiation cavity (hohlraum) with laser beams, creating x-rays. The hohlraum is typically a cylindrical cavity lined with high-Z material such as gold or uranium and filled with helium gas. The 192 laser beams are frequency tripled to a wavelength of 351 nm and enter the hohlraum at the two end caps, passing through the laser-entrance-hole (LEH). Half of the beams enter each LEH, where they subsequently strike the hohlraum wall. The 64 inner beams (23.5° and 30° relative to the hohlraum axis) strike the hohlraum near its equator, and the 128 outer beams (44.5° and 50° relative to the hohlraum axis) are distributed evenly in two rings on the hohlraum wall offset from the central equator. As the lasers deposit their energy, x-rays radiate inward and wall material ablates into the cavity. The helium gas holds the wall back, so that it does not obscure the laser path. However, if the density of the gas is too high, laser-plasma interactions (LPI) can occur, resulting in backscatter of the laser energy. The x-rays created in the wall drive the implosion of a capsule centered in the cavity. For fusion scenarios, the capsule is filled with deuterium and tritium. As the capsule implodes, a hot spot forms, leading to fusion reactions [D + T → α(3.5 MeV) + n(14.1 MeV)]. If the energy within the hot spot is sufficiently confined, the compressed fuel burns. It is the goal of ICF to achieve ignition, a self-sustaining fusion burn, though this has not yet been achieved in the laboratory.

This indirect drive scenario necessarily creates a laser-generated plasma which subsequently generates a magnetic field. This phenomenon has been considered since at least 1971,[1] and it is the subject of a 1991 review article.[2] In it, many different experimental and theoretical papers are discussed, which illustrate the many different ways that self-generated fields can impact the plasma conditions and dynamic evolution of laser-generated plasmas. These include modifying the dynamics of the Rayleigh-Taylor instability and changing the thermal transport properties of the plasma. Further, an imposed magnetic field is an essential part of the MagLIF fusion scheme[3] and has also been proposed as a way to achieve indirect-drive ignition.[4] The understanding of magnetic fields may be important in developing predictive simulation tools for inertial confinement fusion and is also of fundamental physics interest.

In a laser-driven ICF environment, the magnetic pressure created by the self-generated field is typically much smaller than the thermal pressure. For this reason, the plasma $\beta_p = 8\pi p/B^2$ is large, and the hydrodynamic evolution of the plasma is not directly affected by the presence of a magnetic field. The magnetic field can affect the plasma conditions indirectly by altering the heat transport.[5,6] Figure 1

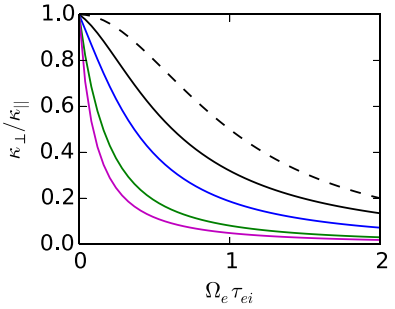

FIG. 1. Ratio of perpendicular to parallel heat conduction in a magnetized plasma vs. Hall parameter, $\Omega_e\tau_{ei}$. Solid black, blue, green, and magenta lines correspond to charge states, $Z = 1$, 2, 8, and ∞, respectively. Dashed black line corresponds to widely used approximation, $[1+\Omega_e^2\tau_{ei}^2]^{-1}$, which understates reduction in heat flow at intermediate values of $\Omega_e\tau_{ei}$.

plots the ratio of electron heat conductivity across the magnetic field, $\kappa_\perp$, to that along the field, $\kappa_{||}$, using the results of Epperlein and Haines.[6] The dashed black line corresponds to the widely used approximation, $[1+\chi^2]^{-1}$, with $\chi \equiv \Omega_e\tau_{ei}$ the Hall parameter, $\Omega_e = eB/m_ec$ the electron cyclotron frequency, and τ_{ei} the electron-ion collision time. This approximation has the correct $\chi = 0$ and $\chi \to \infty$ limits, but understates the reduction in heat flow at intermediate values. This is especially true in the high Z (Lorentz gas) limit, when electron-electron collisions are negligible. Even for $\chi \sim 1$ and modest values of Z, the reduction in heat transport can be as much as 80%–90%.

An accurate description of the self-generated fields in an ICF context connects more broadly to electron heat transport. Fokker-Planck simulation[7–11] is usually considered an adequately first-principles approach to electron transport. These simulations have the advantage of accurately capturing effects due to departures of the distribution function from a Maxwellian[12] and nonlocal effects that exist when $\lambda_e \gtrsim 0.02L_T$, where λ_e and L_T are the electron mean-free-path and temperature scale length, respectively. However, Fokker-Planck descriptions are computationally expensive, and coupling a Fokker-Planck simulation to a radiation-hydrodynamic code would be a formidable task. In practice, flux limiters are typically employed to limit the heat flux from exceeding some fraction of the free-streaming limit, e.g., Ref. 13. This enables the fluid codes to be run in regimes where the fluid approximation, $\lambda_e \ll L_T$, breaks down. The use of flux limiters is problematic, because the flux limiter required for a given experimental situation is not clear *a priori* and likely would vary both temporally and spatially. Understanding the physical origin of flux inhibition and finding an adequate reduced description of the necessary physics is a long-standing project of which this work is a part. Further, magnetic fields and nonlocality are known to interact, e.g., nonlocality can reduce field advection by the Nernst effect.[14] Additionally, magnetohydrodynamic (MHD) simulations of experiments at the Omega laser facility with an imposed magnetic field require a separate flux limiter for the Nernst term to achieve agreement with experimental data.[15] Alternatively, reduced nonlocal models have been developed both with[16] and without[17] magnetic fields, and the use of a reduced nonlocal model has been shown to improve agreement with experimental data.[13,15–18]

This paper aims to explore the consequences of the inclusion of MHD in an integrated ICF simulation. Previous work has considered the effect of an imposed field on capsule performance[4] and hohlraum conditions.[19] Simulations are performed using the radiation-hydrodynamics code HYDRA[20] both with and without MHD[21] included. Here, kinetic and nonlocal effects on heat transport are neglected. This paper illustrates how including MHD alters HYDRA predictions.

This paper is organized as follows. Section II describes the equations governing the magnetic field and heat transport in our extended MHD formalism. This paper reports simulations of three specific experiments. The first two correspond to an undoped high-density carbon (HDC) capsule:[22,23] one with a 0.3 mg/cc helium hohlraum gas fill, and the other with 0.03 mg/cc (a so-called "near-vacuum" hohlraum). These simulations correspond to NIF shots N151122 and N151227,[24] respectively (shot numbers are assigned by date as yymmdd). The third simulation is taken from the high-adiabat or "high foot" campaign,[25] which uses a CH capsule (roughly 30% the density of HDC). This necessitates a much longer laser pulse, due to the longer shock transit-time. The gas fill for this simulation is 0.6 mg/cc. Section III gives an overview of the simulations, and results are reported in Sec. IV. The three experiments are reported as subsections: Secs. IV A, IV B, and IV C correspond to N151122, N151227, and the high foot simulation, respectively. Additionally, a resolution study is reported with the results of N151122, and a comparison of MHD simulations with and without the Nernst term is given with the high foot simulation. Finally, discussion of the simulations and major conclusions are given in Sec. V.

II. SUMMARY OF MHD MODEL

In the notation of Braginskii,[5] later adopted by Epperlein and Haines,[6] the transport equations for a magnetized plasma are

$$en\left(\mathbf{E}+\frac{\mathbf{v}}{c}\times\mathbf{B}\right) = -\nabla p + \frac{\mathbf{j}\times\mathbf{B}}{c} + \frac{\boldsymbol{\alpha}\cdot\mathbf{j}}{en} - n\boldsymbol{\beta}\cdot\nabla T, \quad (1)$$

$$\mathbf{q} = -\boldsymbol{\kappa}\cdot\nabla T - \frac{T\boldsymbol{\beta}\cdot\mathbf{j}}{e}. \quad (2)$$

Here, e is the elementary charge, n is the electron number density, $\mathbf{v}$ is the center-of-mass velocity, $\mathbf{E}$ and $\mathbf{B}$ are the electric and magnetic fields, respectively, p is the electron pressure, $\mathbf{j} = (c/4\pi)\nabla\times\mathbf{B}$ is the current density, and T is the electron temperature. Implicit in writing these equations are the assumptions that gradient length scales are much longer than the collisional mean-free-path of the electrons, and time-scales of interest are long with respect to the collisional and plasma frequencies. This justifies a local, fluid treatment while also allowing for the neglect of the electron inertia. The quantities, $\boldsymbol{\alpha}$, $\boldsymbol{\beta}$, and $\boldsymbol{\kappa}$, are the transport coefficients and correspond to the electrical resistivity, thermoelectric, and thermal conductivity tensors, respectively. These tensor

coefficients can more explicitly be written in component form as

$$\alpha_{ij} = \alpha_{\parallel}\hat{b}_i\hat{b}_j + \alpha_{\perp}(\delta_{ij} - \hat{b}_i\hat{b}_j) + \alpha_{\wedge}\epsilon_{ijk}\hat{b}_k, \tag{3}$$

$$\beta_{ij} = \beta_{\parallel}\hat{b}_i\hat{b}_j + \beta_{\perp}(\delta_{ij} - \hat{b}_i\hat{b}_j) - \beta_{\wedge}\epsilon_{ijk}\hat{b}_k, \tag{4}$$

$$\kappa_{ij} = \kappa_{\parallel}\hat{b}_i\hat{b}_j + \kappa_{\perp}(\delta_{ij} - \hat{b}_i\hat{b}_j) - \kappa_{\wedge}\epsilon_{ijk}\hat{b}_k, \tag{5}$$

with $\hat{\mathbf{b}}$ denoting a unit vector in the direction of the magnetic field, and δ_{ij} and ϵ_{ijk} corresponding to the Kronecker delta and Levi-Civita tensor, respectively. The explicit sign in the anti-symmetric component of the tensor follows the notation of Epperlein and Haines[6] and differs for each term.

If Ohm's law as given in Eq. (1) is substituted into Faraday's law, an equation of motion for the magnetic field results

$$\frac{\partial \mathbf{B}}{\partial t} = \nabla \times \left[\left(\mathbf{v} - \frac{\mathbf{j}}{en}\right) \times \mathbf{B}\right] + \nabla \times \left(\frac{c}{en}\nabla p\right) - \nabla \times \left(\frac{c\boldsymbol{\alpha}\cdot\mathbf{j}}{e^2n^2}\right) + \nabla \times \left(\frac{c\boldsymbol{\beta}\cdot\nabla T}{e}\right). \tag{6}$$

The term, $\nabla \times (\mathbf{v} \times \mathbf{B})$, corresponds to frozen-in advection of the magnetic field. The Hall term, the second term in the square brackets above, causes the magnetic field to advect not at the fluid velocity, but instead, at the electron velocity, $\mathbf{v}_e = \mathbf{v} - \mathbf{j}/en$. The second curl expression in the above equation is the Biermann-Battery term, and its familiar dependence on $\nabla n \times \nabla T$ follows if the equation of state of the electron pressure satisfies $p = nT$. The third curl expression is the resistive diffusion term. The component, $\alpha_{\wedge}$, is a resistive modification to the Hall term. Finally, the thermal term is given in the last expression, of which the Nernst term corresponds to the $\beta_{\wedge}$ component. The Nernst term can be rewritten in terms of an effective advective velocity for the magnetic field, and it corresponds physically to the fact that the magnetic field is advected by heat-carrying electrons moving faster than the bulk.[26] We now assume axisymmetry ($\mathbf{B} = B\hat{\phi}$, $\partial/\partial\phi = 0$), and the magnetic field equation becomes

$$\frac{\partial \mathbf{B}}{\partial t} = \nabla \times \left[\left(\mathbf{v} - \frac{\mathbf{j}}{en}\left(1 + \frac{c\alpha_{\wedge}}{enB}\right) - \frac{c\beta_{\wedge}}{eB}\nabla T\right) \times \mathbf{B}\right] + \nabla \times \left(\frac{c}{en}\nabla p\right) - \nabla \times \left(\frac{c\alpha_{\perp}\mathbf{j}}{e^2n^2}\right) + \nabla \times \left(\frac{c\beta_{\perp}\nabla T}{e}\right). \tag{7}$$

Since the magnetic field lies in the direction of symmetry, none of the parallel transport coefficients appears. To further simplify the equation, it is assumed that the plasma pressure is much greater than the magnetic pressure, i.e., $\beta_p = 8\pi nT/B^2 \gg 1$. The ratio of the Hall velocity, $j/en \sim cB/4\pi enl_B$, to the Nernst velocity, $c\beta_{\wedge}T/eBl_T$, is $(2/\beta_p)(l_T/l_B\beta_{\wedge})$. Here, l_B and l_T are the magnetic and temperature gradient scale lengths, respectively. The factor of β_p in the denominator suggests that the Hall term is of less importance for high β_p plasmas, and it is not included in the simulations reported herein. Additionally, the thermal term, containing the $\beta_{\perp}$ coefficient, is neglected as it only enters through gradients present in the coefficient itself. This leads to the following reduced equation which is modeled in the simulations reported here

$$\frac{\partial \mathbf{B}}{\partial t} = \nabla \times \left[\left(\mathbf{v} - \frac{c\beta_{\wedge}}{eB}\nabla T\right) \times \mathbf{B}\right] + \nabla \times \left(\frac{c}{en}\nabla p\right) - \nabla \times \left(\frac{c\alpha_{\perp}\mathbf{j}}{e^2n^2}\right). \tag{8}$$

In modeling the electron heat transport, Eq. (2.3e) of Ref. 5 can be written as

$$\frac{3}{2}n\frac{dT}{dt} + p\nabla\cdot\mathbf{v}_e = -\nabla\cdot\mathbf{q} + Q, \tag{9}$$

where viscous terms have been neglected. Additional source terms, such as laser absorption and x-ray deposition, are included in the simulations but are not discussed here. The convective derivative is given by $d/dt = \partial/\partial t + \mathbf{v}_e\cdot\nabla$. The heat flux, $\mathbf{q}$, is given by Eq. (2), and the heat deposited in the electrons can be generalized from Eqs. (2.18), (4.30), and (4.31) of Ref. 5 as

$$Q = \mathbf{j}\cdot\left(\frac{\boldsymbol{\alpha}}{e^2n^2}\cdot\mathbf{j}\right) - \frac{\mathbf{j}}{en}\cdot(\boldsymbol{\beta}\cdot\nabla T) + \frac{3m_e}{m_i}\frac{n}{\tau_{ei}}(T_i - T). \tag{10}$$

Making the same two-dimensional assumption, the electron heat equation reduces to

$$\frac{3}{2}n\frac{dT}{dt} + p\nabla\cdot\mathbf{v}_e = \frac{\alpha_{\perp}j^2}{e^2n^2} + \nabla\cdot\left[\kappa_{\perp}\nabla T + \frac{T}{e}\beta_{\wedge}\hat{\mathbf{b}}\times\mathbf{j}\right] - \frac{\mathbf{j}}{en}\cdot\beta_{\wedge}\hat{\mathbf{b}}\times\nabla T + \frac{3m_e}{m_i}\frac{n}{\tau_{ei}}(T_i - T) + \nabla\cdot\left[\kappa_{\wedge}\hat{\mathbf{b}}\times\nabla T + \frac{T}{e}\beta_{\perp}\mathbf{j}\right] - \frac{\mathbf{j}}{en}\cdot\beta_{\perp}\nabla T. \tag{11}$$

The terms on the right-hand side in the above equation correspond sequentially to resistive heating, thermal conduction, two terms proportional to the Nernst coefficient, $\beta_{\wedge}$, collisional relaxation with the ions, the Righi-Leduc portion of the heat-flux, and the perpendicular thermo-electric tensor. The terms in the last line are not included in the HYDRA simulations. The Righi-Leduc term may be relevant, and effort should be made to explore its effects, though it is outside the scope of this paper. Physically, it carries heat flux at right angles to both the temperature gradient and the magnetic field, and at large degrees of magnetization, it is the dominant component of the heat flux.

III. SIMULATION OVERVIEW

In performing the simulations, three different experimental conditions were simulated. The laser power for each of these shots is given in Fig. 2 with the blue and green curves corresponding to NIF shots N151122 and N151227, respectively. The red curve corresponds to a high foot simulation. NIF shots N151122 and N151227 have an HDC capsule with a short laser pulse, and they are modeled as

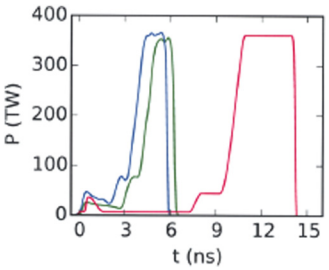

FIG. 2. Total laser power vs. time. Blue and green curves correspond to NIF shots N151122 and N151227 (HDC capsule); red curve corresponds to a high foot simulation (CH capsule). Longer pulse length of red curve is due to different ablator thicknesses and different initial shock pressures in CH.

post-shots with the actual laser power used. The high foot simulation uses a CH capsule. Experimental parameters are summarized in Table I. In all simulations, the high-flux model is adopted.[13] This consists of a DCA atomic physics package of the high Z wall[27] and an electron heat flux limiter of $\lambda = 0.15$. Here, DCA refers to the atomic kinetic implementation as constructed in Ref. 27. In implementing the flux limiter with the inclusion of magnetic fields, only the thermal conduction is limited. This is done in each index direction, $\mathbf{e}_k$, independently so that $|\mathbf{q}_T \cdot \mathbf{e}_k| = \min[|\kappa_{ij} e_{k,i} \nabla_j T|, \lambda q_{FS}]$, where $q_{FS} = nT^{3/2}/m_e^{1/2}$ is the free-streaming heat flux. The low gas-fill densities considered here decrease the level of LPI to a degree that they should have negligible effects on the energetics of the simulation, and for this reason, no model of LPI is included. Since the first two simulations use the as-shot laser power, the small amount of experimentally observed backscatter is subtracted from the incident laser energy. Since all of these shots used the same frequency for all beams, no model for cross beam transfer is included.

Additionally, it is a common practice to utilize time-dependent laser-power multipliers[28] to reduce the power entering the hohlraum. This is done because the measured x-ray drive is lower than calculated when using the high flux model; this is often referred to as the "drive deficit." Here, the multipliers for the HDC capsule simulations are chosen to match simulations without MHD to shock-timing data from experiments. For N151122 and N151227, the multipliers at peak power are 0.86 and 0.9, respectively. For the CH simulation, the multiplier is 0.9 throughout the laser pulse. However, for a given experiment, the simulations with and without MHD utilized the same set of laser-power multipliers. Therefore, in interpreting the results reported here, the meaningful comparison is between simulations with and without MHD, though experimental values are reported for reference.

TABLE I. Simulation parameters.

	N151122	N151227	High foot
Laser energy (MJ)	0.788	0.771	1.626
Hohlraum He fill density (mg/cc)	0.3	0.032	0.6
Hohlraum diameter (mm)	5.75	5.75	6.72
Hohlraum length (mm)	10.1	10.1	11.24
LEH diameter (mm)	3.37	3.37	3.64
Ablator	HDC	HDC	CH
Hohlraum material	U	Au	U

One difficulty in performing MHD simulations with the Biermann-Battery term is the presence of Biermann catastrophe,[29,30] which is a numeric failure of MHD that occurs when the Biermann generated magnetic field strength diverges with increasing grid resolution. This occurs at discontinuities in plasma conditions such as occur in a shock. This gives unphysical results, occurring even in spherically symmetric shocks where no Biermann field is generated. A simple solution for addressing this problem is to simply turn off the Biermann source term when a shock is detected.[29] A more physical approach rederives the Rankine-Hugoniot jump conditions in the presence of a magnetic field and then ensures that the jump in magnetic field across a shock is computed correctly.[30] This latter approach is not suitable in HYDRA simulations of integrated ICF targets simply because the required resolution to apply the formalism is too great to make the simulations tractable. For this reason, the former approach is adopted. When the gradient length scale of the velocity, $L_v = |\mathbf{v}|/|\nabla \cdot \mathbf{v}|$, exceeds a specified fraction, η, of the longest length between two nodes of a given zone, L_{cell}, the Biermann term is turned off, i.e., when $L_v/L_{\text{cell}} > \eta$. Here, $\eta = 0.1$ throughout the manuscript.

IV. SIMULATION RESULTS

A. N151122 (HDC capsule, 0.3 mg/cc fill)

In analyzing N151122, we first wish to illustrate that the MHD package is numerically convergent and is working in a reasonable manner. Given the concern about Biermann catastrophe in previous simulations, this exercise is an important step to give the results credibility. For this reason, a resolution study is first performed. Two quantities were varied in tandem: the angular zoning and the radial resolution in the hohlraum wall. Figure 3 illustrates the hohlraum geometry with the coarsest resolution used in this study shown on the top right panel. Because of the symmetry plane that exists at $z = 0$, all the simulations here are one-sided, amounting to $z > 0$. We extend the radial coordinate to negative values for understanding purposes only, but in reality, the top right panel is simulated as a wedge with periodic boundary condition in the azimuthal direction to represent the full figure of revolution. For these reasons, quadrants II, III, and IV have increased transparency. In quadrant I, the angular zoning is broken into six regions. The first region is given by the red mesh and has 28 zones in the angular direction. The black mesh (8 zones) captures the bend in the hohlraum. The pink mesh (2 zones) is the straight section of the hohlraum; in uranium hohlraums, the uranium ends at the end of this mesh. The blue mesh (4 zones) is the straight section of the gold end cap which is present even on uranium hohlraums. The orange mesh (10 zones) corresponds to the hook transitioning from the hohlraum to the LEH. Finally, the green mesh (12 zones) corresponds to the LEH window. When varying the angular zoning of the hohlraum in this manuscript, the number of zones shown is increased by factors of two and four. All resolutions are increased except the green mesh which is kept fixed. This portion of the mesh is unlikely to affect the physics occurring deeper in the hohlraum. Thus, if the 12 zones in the LEH are not included in

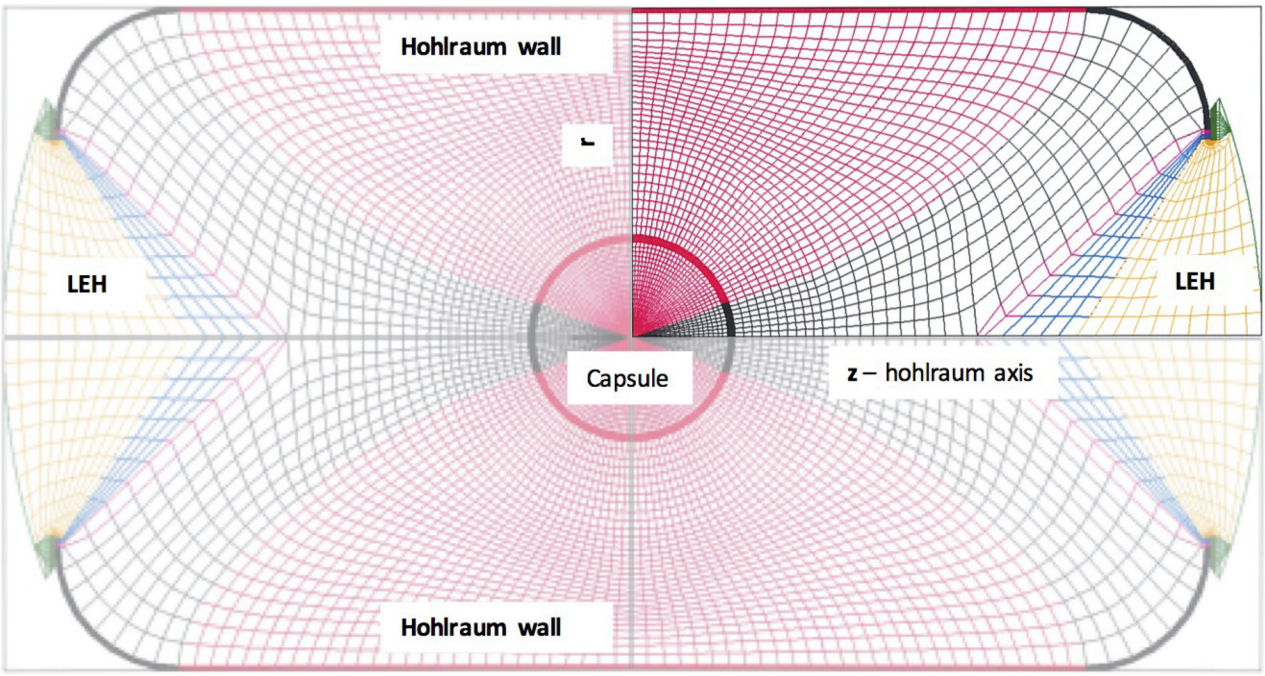

FIG. 3. Cross-section of hohlraum with various features labeled. Initial mesh at coarsest resolution for half a hohlraum is given in quadrant I. Horizontal and vertical axes correspond to radius and axis of hohlraum, respectively. Features of hohlraum are labeled. Different colors partition mesh into distinct regions: red (straight portion of hohlraum), black (bend in hohlraum), pink (straight portion of hohlraum cap, variable material), blue (straight portion of hohlraum cap, always composed of gold), orange (transition to hook), and green (window).

the number of angular zones, N_θ, then the coarsest resolution corresponds to $N_\theta = 52$. Additionally, the number of photons used in the radiation portion of the computation is also increased by the same factor in order to keep the photons per zone constant.

The radial zoning is also varied in the hohlraum wall. The simulation is set up so that the first radial zone in the hohlraum is 40 Å thick, and each successive zone increases by some fraction of the previous zone, i.e., $\Delta r_{j+1} = \nu \Delta r_j$. In the coarsest case, $\nu = 1.1$, so that the width between zones increases by 10% with each cell. Two additional runs are done with $\nu = 1.05$, $N_\theta = 104$ and $\nu = 1.025$, $N_\theta = 208$, decreasing the radial ratio as the angular resolution also increases. Decreasing the value of ν increases the number of radial zones in the hohlraum wall as follows: $N_r = 72$, 132, and 234, respectively.

The resolution scan is done both with and without MHD for NIF shot N151122. In an integrated simulation such as this where many differing quantities are tracked, the degree of convergence can be assessed in many different ways. In this study, convergence is measured in terms of two physical quantities. First, the gross energetics of the simulation are assessed simply in terms of the bang-time of the simulation, as determined by the time of peak neutron production. Second, the increase in temperature of the hohlraum plasma decreases absorption by the laser beam, allowing the inner beams to propagate further into the plasma and deposit their energy closer to the waist of the hohlraum. This leads to increased X-ray drive near the midplane, resulting in a more prolate implosion. The impact of this effect is captured by the amount of P_2/P_0, where P_n represents the coefficients from a Legendre decomposition of the implosion shape.

The results are shown in Fig. 4. In the top panel, the variation in the simulated neutron bang-time relative to the experimental value[31,32] is plotted as a function of ν. For reference, the experimental bang-time is 7.4 ± 0.1 ns. In the

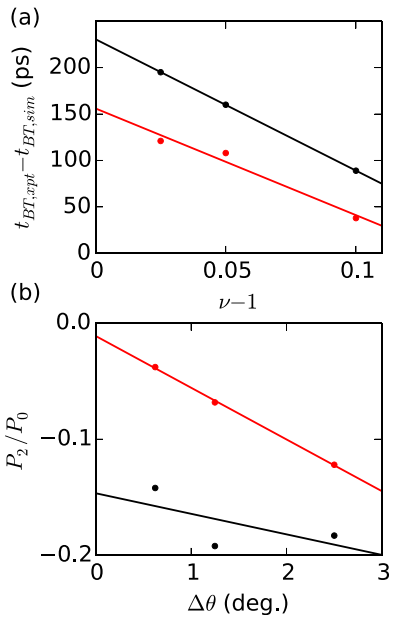

FIG. 4. Convergence of bang-time and P_2/P_0 in simulations of N151122. (a) Difference in experimental and simulated bang-time vs. $\nu - 1$, where ν corresponds to increasing ratio of radial zoning in hohlraum wall. Experimental bang-time is 7.4 ± 0.1 ns. (b) P_2/P_0 asymmetry vs. angular resolution in degrees. Experimental value is $(-0.1 \pm 9.4)\%$. Red and black points correspond to simulations with and without the MHD package, respectively. Lines are least-squares fits to the simulated data. In convergence study, $\nu - 1$ and $\Delta\theta$ are varied in tandem by factors of two, so the horizontal axes on the top and bottom panels are interchangeable.

plot, a positive time difference corresponds to a simulated bang-time occurring earlier than that observed in the lab. The bottom panel shows the simulated P_2/P_0 ratio as a function of the angular resolution, $\Delta\theta$ near the capsule. For reference, the measured value is $(-0.1 \pm 9.4)\%$. The red and black points in both panels correspond to simulations with and without MHD, respectively. The top panel was plotted as a function of ν simply because the energetics of the capsule are most likely sensitive to the radial zoning of the hohlraum wall, as it is the X-ray radiation of the wall material that determines the drive on the capsule. Similarly, the symmetry shown in the bottom panel is plotted as a function of $\Delta\theta$ as it determines the angular resolution of the inner-beam laser-power deposition, altering the implosion shape. However, since both ν and $\Delta\theta$ are varied in lock-step by factors of two, the horizontal axes of the top and bottom panels are interchangeable.

For general convergent numeric schemes, a scalar quantity, y, converges according to

$$y_h = y_0 + ch^p, \tag{12}$$

where y_0 is the converged result, c is an arbitrary constant, h is a spatial or temporal step that is being varied, and p is the order of convergence. For a given simulation, three different step sizes can be used: h, $h/2$, and $h/4$, and this allows for the determination of y_0, c, and p in the above equation through Richardson extrapolation, with an error of order h^{p+1} due to the neglect of higher order terms. In the integrated simulations reported here, it possible to vary many different resolution parameters. This is further complicated by the use of an arbitrary-Lagrangian-Eulerian mesh of varying cell size and an adaptive time-step used throughout the simulation. For this reason, too much rigor in this regard is inappropriate, and a detailed convergence study is outside the scope of this manuscript. However, given the positioning of the points in Fig. 4, linear convergence is assumed ($p = 1$), and the corresponding solid lines in the figure are a linear least-squares fit to the simulation results. From the fit, an extrapolation can be performed to determine an estimate of the bang-time and P_2 shape of a perfectly resolved simulation. The simulated bang-times of the converged result are estimated to be 230 ps (no MHD) and 147 ps (MHD) before the experimental bang-time, and the P_2 asymmetry is -14.7% (no MHD) and -1.1% (MHD). The DCA atomic physics package and power multipliers are being used, both of which are likely to have a greater impact on bang-time than what is observed by including MHD. This does, however, show convergence of the MHD package in its present form.

Examining the hohlraum plasma conditions for the finest resolution case, a contour plot of the electron temperature in keV at $t = 5$ ns is shown in Fig. 5. The top panel plots the absolute temperature for the two simulations: $r > 0$ corresponds to the simulation with the MHD package, and $r < 0$, without the MHD package. The bottom panel plots the temperature difference between the two simulations with positive values corresponding to a hotter MHD result. The simulations are performed as one-sided hohlraums, assuming a plane of symmetry at z = 0. The capsule is located at the origin with the laser beams entering the hohlraum from the LEH window on the right of the figure. The horizontal and vertical axes are the axial and radial coordinates, respectively, with positive radius corresponding to the MHD simulation and negative radius, to the simulation without MHD. The black curve is a contour of average atomic weight, $\bar{A} = 15$, representing the transition between the lighter helium, $A = 4$, and the much heavier wall material. The wall bubble formed by the power deposition of the outer beams is clearly evident from the shape of the contour, and it is responsible for partially obscuring the paths of the inner beams. From the filled contours, it is clear that the wall bubble in the MHD simulation is roughly 1 keV hotter than when MHD is neglected. This decreases the inverse Bremsstrahlung of the inner beams as they propagate through the wall bubble, allowing them to deposit their energy closer to the midplane of the hohlraum. The ultimate consequence of this is the shift towards a more prolate shape of the implosion as shown by the difference between the red and black curves in Fig. 4.

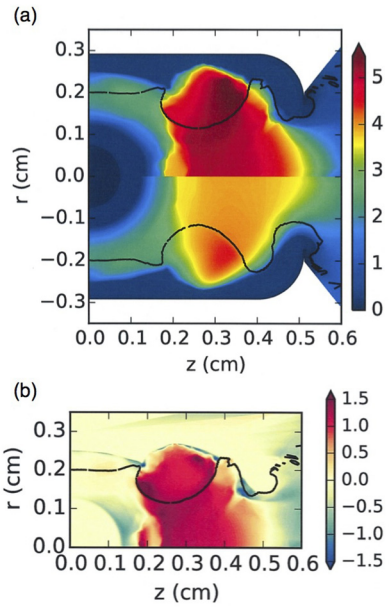

FIG. 5. Contour plot of T_e (keV) in simulation of N151122 (HDC capsule, 0.3 mg/cm^3 fill) at $t = 5$ ns (near end of peak power). (a) Electron temperature. Positive (negative) radius corresponds to simulation with (without) MHD. (b) Temperature difference between top and bottom panels of (a). Black contours are made at average atomic mass, $\bar{A} = 15$, illustrating boundary between light helium gas and denser wall material. MHD simulation shows increase in electron temperature in gold bubble and helium gas due to reduction in heat transport caused by magnetization of plasma.

The azimuthal component of the magnetic field measured in megagauss is also plotted in Fig. 6. This plot is made at the same time as Fig. 5 on the same axes, and the black contour illustrates the interface between the wall material and the helium gas in the hohlraum as before. The azimuthal direction is out of the page, with positive (negative) values of B_ϕ being directed out of (into) the page. The megagauss magnetic fields, while originating in the underdense wall material are advected towards the denser wall material where they are dissipated in a colder, more collisional region. There are similarly large fields observed both in the

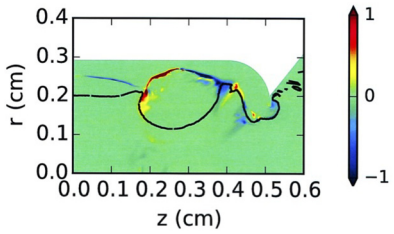

FIG. 6. B_ϕ (MG) in simulation of N151122 with MHD at $t = 5$ ns (near end of peak power). Black contour illustrates interface between heavy wall material and lighter helium gas. Large magnetic fields appear at interface between dense wall and underdense, ablative blow off due to large self-generated magnetic fields in this region. Nernst flow advects magnetic fields towards the hohlraum wall. Large magnetic fields are also present in LEH.

LEH and along the wall closer to the midplane of the hohlraum. To illustrate the reduced heat conductivity, a corresponding plot of the Hall parameter, $\chi = \Omega_e \tau_{ei}$, is made in Fig. 7. The dark red region is off the scale of the colorbar, indicating that there are regions surrounding the wall bubble and LEH with large Hall parameter. This shows that although the field is smaller than in the wall, the larger τ_{ei} results in a larger χ and a greater reduction in the heat flux. Note the blue line of Fig. 1 where even for a modest value of $\chi = 2$, the heat conduction in a helium ($Z = 2$) plasma is reduced by roughly 90%.

B. N151227 (HDC capsule, 0.032 mg/cc fill)

Next, the simulation of NIF shot N151227 is considered. This simulation is performed with the coarsest resolution used in Sec. IV A. This is done for convenience in order to reduce the computational expense of the simulation and decrease potential for mesh tangling. From the resolution scan, improving the resolution changes bang-time by ∼100 ps and a 10% shift in the prolate direction of the P_2 asymmetry, while other quantities such as the magnetic field and electron temperature will also slightly change from their unresolved values. Qualitatively, though, the comparison between MHD and no MHD simulations is still valid as convergence did not eliminate their differences. The electron temperature at $t = 6$ ns is plotted in Fig. 8 with the top panel corresponding to the simulation with the MHD package, and the bottom, without, as before. Qualitatively, Fig. 8 is similar to Fig. 5, except that in the former, the contour denoting the

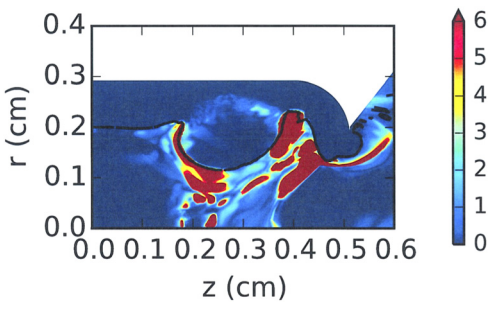

FIG. 7. Hall parameter, $\chi = \Omega_e \tau_{ei}$, in simulation of N151122 with MHD at $t = 5$ ns. Black contour illustrates interface between heavy wall material and lighter helium gas. Large regions of domain have $\chi > 1$, leading to sharp reduction in heat conduction (see Fig. 1). Relatively small values of B_ϕ in the helium plasma (see Fig. 6) lead to large values of χ due to much larger τ_{ei}.

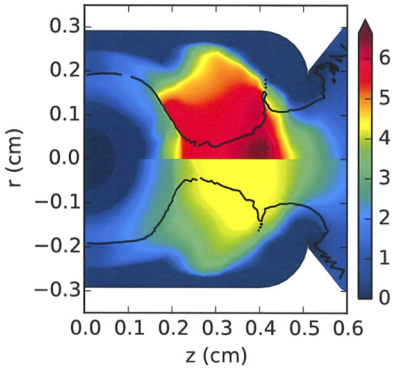

FIG. 8. Contour plot of T_e (keV) in simulation of N151227 (HDC capsule, 0.032 mg/cc fill) at $t = 6$ ns. Black contour, illustrating boundary between wall bubble and helium gas, extends farther into hohlraum than in Fig. 5 due to order of magnitude lower initial gas fill density. Positive (negative) radius corresponds to simulation with (without MHD). Similar temperature profile and temperature increase with MHD to simulation of N151122.

boundary between the wall material and the helium gas extends much further into the hohlraum. This is simply due to the order of magnitude lower gas fill present in NIF shot N151227. The temperature differences between the two shots are similar within the wall bubble, but are more extreme within the helium plasma towards the axis. This can also be attributed to differences in gas fill; a small amount of energy trapped within the lower density plasma will result in a larger temperature increase. The impact of the increase in electron temperature when using the MHD package has a similar impact on bang-time and the simulated P_2 asymmetry to that observed in N151122: bang-time is 8.16 ns (no MHD) and 8.23 ns (MHD), and P_2/P_0 is −34.3% (no MHD) and −24.6% (MHD). For reference, the experimental data gave an X-ray bang-time of 8.22 ± 0.06 ns and an observed P_2/P_0 of (+30.5±4.0)%.[24]

C. High foot (CH capsule, 0.6 mg/cc fill)

Next, the high foot simulation (CH capsule 0.6 mg/cm^3 and roughly twice the laser energy) is considered. This simulation similarly used the coarsest resolution as in N151227. Again, an increase in electron temperature is observed as shown in Fig. 9. Here, the electron temperature plot is made at $t = 13$ ns. Quadrants I and IV again correspond to the simulation with and without the MHD package, respectively. The temperature differences are similar to those shown in the previous two simulations, with a peak temperature of roughly 5.5 keV with MHD and 4.5 keV without MHD. The higher gas fill density in this simulation holds back the wall more effectively, resulting in less displacement of the black contour from its initial location. The temperature profile has shifted slightly towards the LEH as compared to the previous simulations. This is evident if one compares either the top (with MHD) or the bottom (no MHD) panels of Figs. 5, 8, and 9. This is likely due to the difference in the laser pulse as shown in Fig. 2. Extending the temporal length of the laser allows for increased hydrodynamic motion, allowing the plasma to advect towards the LEH carrying thermal energy with it. The increase in plasma temperature has qualitatively similar effects on bang-time and P_2/P_0 asymmetry: the

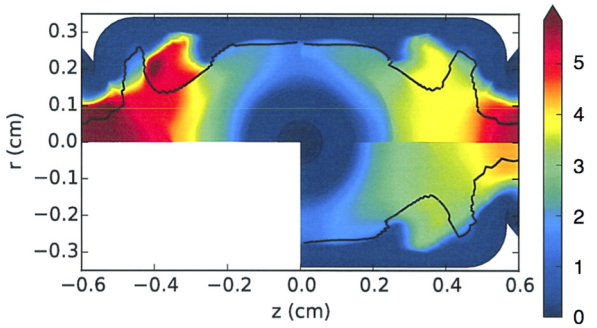

FIG. 9. Contour plot of T_e (keV) in high foot simulation (CH capsule, 0.6 mg/cc fill) at $t = 13$ ns (near end of peak power). Black contour, illustrating boundary between wall bubble and helium gas, does not extend as far as in Fig. 5 due to larger initial gas fill density. Quadrants I (Nernst on) and II (Nernst off) are both MHD simulations. Quadrant IV is without MHD. Quadrant II is saturated with the peak temperature slightly above 7 keV. Comparing MHD with Nernst to no MHD, temperature peak shifted towards LEH likely because of additional time for hydrodynamic flow due to longer laser pulse. Qualitatively similar temperature increase between MHD with Nernst and no MHD simulation to that observed in Figs. 5 and 8.

bang-time is 14.66 ns (MHD) and 14.67 ns (no MHD), and the P_2/P_0 asymmetry is 46.3% (MHD) and −0.3% (no MHD). The greater symmetry swing can be explained by the longer pulse duration at peak power; in the high foot simulation, the duration of peak power is roughly twice as long. The differences in inner beam propagation due to the change in electron temperature between the MHD and no MHD simulation increase with time. In all cases, the increased electron temperature results in improved propagation of the inner beams shifting the symmetry. Figure 9 additionally includes a simulation with MHD but excluding advection by the Nernst term. Because the magnetic field is not carried into the denser wall material, it reduces the heat conduction by a larger amount leading to even greater temperatures, as shown in quadrant II. Here, the temperature profile is qualitatively similar but with greater plasma temperatures everywhere. The peak temperature in this case is 7 keV, which is off-scale, all contour plots having been scaled to the peak temperature in quadrant I.

To examine the effect of the Nernst term and to see if the package is behaving as expected, a simulation is performed comparing three runs: MHD, MHD without the Nernst term, and no MHD. Simulations without the Nernst effect neglect any term in Eqs. (8) and (11) which are proportional to $\beta_\wedge$. Figure 10 plots B_ϕ (MG) from the MHD simulation in the top panel with lineouts of B_ϕ (MG) and T_e (keV) in the bottom panel. The lineouts are made at $z =$ 0.3 cm as indicated by the vertical goldenrod line. In the bottom panel, the red curves correspond to the left, vertical axis plotting magnetic field, and the blue curves correspond to the right vertical axis plotting electron temperature. The solid, dashed, and dashed-dotted curves correspond to the MHD, MHD without Nernst, and no MHD simulations, respectively. There is no red dashed-dotted line because, without MHD, there is no magnetic field in the simulation. The black lines at the top of the plot divide the radius into three intervals of dominant ion species: from left to right, helium, gold, and uranium. From the lineout of the magnetic field, it is

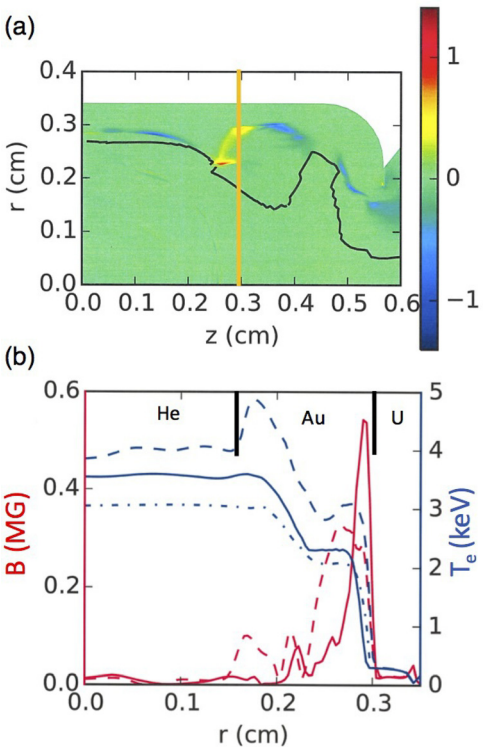

FIG. 10. (a) Contour plot of B_ϕ (MG) for high foot simulation at $t = 13$ ns (near end of peak power) for MHD simulation with Nernst term. Goldenrod line illustrates lineout plotted in lower panel. (b) Lineout of $|B|$ (MG) and T_e (keV) at $z = 0.3$ cm. Red curves correspond to $|B|$ (left axis); blue curves to T_e (right axis). Solid and dashed lines correspond to full MHD and MHD without Nernst simulations, respectively. The dashed-dotted line corresponds to without MHD simulation and has no red line for this reason. Black lines divide radius into intervals of dominant ion species (He, Au, or U) as labeled. Nernst advection moves magnetic field into wall (larger radius) and correspondingly decreases electron temperature.

clear that the Nernst effect advects the magnetic field into the colder dense wall as expected. The temperature plots illustrate the role the Nernst term plays in indirectly affecting the heat transport. The exclusion of any magnetic field results in the coldest plasma of the three simulations. Adding MHD but without the Nernst term results in much hotter plasma, increasing the temperature by roughly 2 keV in the gold bubble. Upon including Nernst advection in the simulation, the magnetic field strength decreases in the gold bubble and in the plasma enhancing the heat transport, but not to the level present in the no MHD simulation. Thus, the MHD with Nernst simulation is hotter (but less so) than the no MHD simulation. Further, the bang-time and P_2/P_0 for the MHD without Nernst simulation are 14.71 ns and 59.6%, respectively. This is a dramatic effect and indicates the sensitivity of the result to the Nernst term, or more broadly, the location of the magnetic field.

V. CONCLUSION

In summary, this paper reports integrated ICF simulations for NIF targets which include the effects of MHD through the Biermann-battery, Nernst, resistive, and anisotropic heat conduction terms. A convergence study is performed to illustrate the numeric convergence of the MHD package. It is shown that the inclusion of MHD results in a

hotter simulated hohlraum plasma, which leads to enhanced propagation of the inner beams towards the midplane. Three shots are considered: N151122, N151227, and a high foot simulation. The simulation for N151122 brings the predicted shape into agreement with experimental data. The simulation for N151227 results in a P_2/P_0 of -25% while the experimental data is $+30\%$. Such a discrepancy is typical of previous results for near-vacuum hohlraums, and an *ad hoc* enhanced beam propagation model (artificially increasing the frequency of the inner beams) has been used to bring the simulations in agreement with the experiments.[23] For a similar experiment, it was necessary to increase the simulated inner beam frequency from 3ω light (351 nm) to 5ω (211 nm).[23] The results here show that while MHD does improve propagation of the inner beams, it does not remove the discrepancy. It may be necessary to account for interpenetration between the wall material and the ablator in order to remove the need for an enhanced propagation model. The high foot simulation behaves qualitatively similar to the two HDC simulations, with the temperature peak shifted towards the LEH. This can be explained by the difference in pulse shape. The inclusion of MHD did not significantly alter the simulated bang-time, and for this reason, it is unlikely to explain the drive deficit observed in NIF experiments. In all three simulations, a hotter hohlraum plasma is observed with a shift to more prolate shape by 14% (N151122), 10% (N151227), and 46% (high foot).

Davies[15] performed MHD simulations of experiments performed on the Omega laser facility with an imposed magnetic field. To gain agreement with experimental data, an additional flux-limiter was imposed on Nernst advection. Because Nernst advection is proportional to the heat flux, unmodeled physics (such as nonlocality) that reduces the heat flux will also reduce the Nernst velocity. In this work, Nernst advection of the field is either on or off, with no intermediate reduction below the fluid-Braginskii result. Reduction of Nernst advection is examined here by additionally neglecting Nernst advection in the high foot case, showing the maximum possible reduction of Nernst motion. This bounds the effect of reduced Nernst motion. The high-foot simulation with Nernst flow turned off results in the underdense plasma electron temperature increasing from the no MHD simulation by 2 keV or more, reaching 7 keV in the LEH. This occurs because the magnetic fields remain in the underdense plasma instead of being advected into the colder, denser, more resistive wall. Within the wall, the confinement of heat flow by the magnetic field is not as pronounced because electron-ion collisions occur with much greater frequency, reducing the value of χ and increasing the resistivity of the material, subsequently dissipating the fields. At temperature differences of this magnitude, the shift in bang-time is still less than 100 ps. This indicates that, even with reduced Nernst advection, MHD is unlikely to remove the need for drive multipliers to match shock-timing data. The three types of simulations (standard, MHD with Nernst, and MHD without Nernst) give different enough predictions of electron temperature that comparisons to experimental data should be able to constrain the electron heat transport model and the manner in which the MHD package is employed. This will also enable the future investigation of the underlying physics governing the Nernst speed. Reduction of Nernst advection would also result in intermediate electron temperatures between simulations with and without the Nernst effect.

In all of the results reported here, the high flux model has been employed.[13] This has two main ingredients: a large heat flux limiter of 0.15 and the DCA atomic physics package. A heat flux limiter is an *ad hoc* assumption in order to remove the necessity of capturing nonlocal effects on heat transport. It is possible that the effects of magnetic fields could be approximately modeled by simply lowering the flux limiter, resulting in a larger plasma temperature. However, this lower flux limiter is imposed in a predetermined way, while the magnetic field and corresponding Hall parameter and heat conduction vary according to the dynamics of the plasma itself. This shows the interplay between MHD and electron heat transport. The second part of the high flux model, a DCA atomic physics package, also has its own uncertainties that are greatest at large Z. In order to disentangle deficiencies in the atomic physics model from those in the electron heat transport, further work should benchmark Fokker-Planck simulations[7] against single-fluid HYDRA simulations. This would further elucidate the possible importance of nonlocal transport and ion-acoustic turbulence[33] on hohlraum plasma conditions. Further, investigation into the adequacy of reduced nonlocal descriptions that also include the effects of MHD[16] would be helpful. Additionally, comparisons to experiment are vital. In this vein, using mid Z materials where the atomic physics is better understood would allow the deficiencies of the atomic physics to be disentangled from deficiencies in heat transport. Comparisons to dot-spectroscopy[34] or proton radiography[35] measurements would also constrain the models.

ACKNOWLEDGMENTS

The authors are grateful to G. B. Zimmerman, J. A. Harte, and M. M. Marinak for constructive comments regarding the content of this manuscript. This work was performed under the auspices of the U.S. Department of Energy by Lawrence Livermore National Laboratory under Contract No. DE-AC52-07NA27344.

[1]J. A. Stamper, K. Papadopoulos, R. N. Sudan, S. O. Dean, E. A. McLean, and J. M. Dawson, Phys. Rev. Lett. **26**, 1012 (1971).
[2]J. A. Stamper, Laser Part. Beams **9**, 841 (1991).
[3]S. A. Slutz and R. A. Vesey, Phys. Rev. Lett. **108**, 025003 (2012).
[4]L. J. Perkins, B. G. Logan, G. B. Zimmerman, and C. J. Werner, Phys. Plasmas **20**, 072708 (2013).
[5]S. I. Braginskii, "Transport processes in a plasma," in *Reviews of Plasma Physics* (Consultants Bureau, New York, 1965), Vol. 1, pp. 205–311.
[6]E. M. Epperlein and M. G. Haines, Phys. Fluids **29**, 1029 (1986).
[7]A. G. R. Thomas, M. Tzoufras, A. P. L. Robinson, R. J. Kingham, C. P. Ridgers, M. Sherlock, and A. R. Bell, J. Comput. Phys. **231**, 1051 (2012).
[8]M. Tzoufras, A. R. Bell, P. A. Norreys, and F. S. Tsung, J. Comput. Phys. **230**, 6475 (2011).
[9]M. Tzoufras, A. Tableman, F. S. Tsung, W. B. Mori, and A. R. Bell, Phys. Plasmas **20**, 056303 (2013).
[10]A. S. Joglekar, A. G. R. Thomas, W. Fox, and A. Bhattacharjee, Phys. Rev. Lett. **112**, 105004 (2014).

[11]A. S. Joglekar, C. P. Ridgers, R. J. Kingham, and A. G. R. Thomas, Phys. Rev. E **93**, 043206 (2016).
[12]A. B. Langdon, Phys. Rev. Lett. **44**, 575 (1980).
[13]M. D. Rosen, H. A. Scott, D. E. Hinkel, E. A. Williams, D. A. Callahan, R. P. J. Town, L. Divol, P. A. Michel, W. L. Kruer, L. J. Suter *et al.*, High Energy Density Phys. **7**, 180 (2011).
[14]J. F. Luciani, P. Mora, and A. Bendib, Phys. Rev. Lett. **55**, 2421 (1985).
[15]J. R. Davies, R. Betti, P.-Y. Chang, and G. Fiksel, Phys. Plasmas **22**, 112703 (2015).
[16]P. D. Nicolaï, J.-L. A. Feugeas, and G. P. Schurtz, Phys. Plasmas **13**, 032701 (2006).
[17]G. P. Schurtz, P. D. Nicolaï, and M. Busquet, Phys. Plasmas **7**, 4238 (2000).
[18]L. Lancia, B. Albertazzi, C. Boniface, A. Grisollet, R. Riquier, F. Chaland, K.-C. Le Thanh, P. Mellor, P. Antici, S. Buffechoux *et al.*, Phys. Rev. Lett. **113**, 235001 (2014).
[19]D. J. Strozzi, L. J. Perkins, M. M. Marinak, D. J. Larson, J. M. Koning, and B. G. Logan, J. Plasma Phys. **81**, 475810603 (2015).
[20]M. M. Marinak, G. D. Kerbel, N. A. Gentile, O. Jones, D. Munro, S. Pollaine, T. R. Dittrich, and S. W. Haan, Phys. Plasmas **8**, 2275 (2001).
[21]J. M. Koning, G. D. Kerbel, and M. M. Marinak, in *APS Meeting Abstracts* (2011), Vol. 1, p. 9115P.
[22]A. J. MacKinnon, N. B. Meezan, J. S. Ross, S. Le Pape, L. Berzak Hopkins, L. Divol, D. Ho, J. Milovich, A. Pak, J. Ralph *et al.*, Phys. Plasmas **21**, 056318 (2014).
[23]L. F. Berzak Hopkins, S. Le Pape, L. Divol, N. B. Meezan, A. J. Mackinnon, D. D. Ho, O. S. Jones, S. Khan, J. L. Milovich, J. S. Ross *et al.*, Phys. Plasmas **22**, 056318 (2015).
[24]D. Turnbull, L. F. B. Hopkins, S. Le Pape, L. Divol, N. Meezan, O. L. Landen, D. D. Ho, A. Mackinnon, A. B. Zylstra, H. G. Rinderknecht *et al.*, Phys. Plasmas **23**, 052710 (2016).
[25]D. E. Hinkel, L. F. B. Hopkins, T. Ma, J. E. Ralph, F. Albert, L. R. Benedetti, P. M. Celliers, T. Döppner, C. S. Goyon, N. Izumi *et al.*, Phys. Rev. Lett. **117**, 225002 (2016).
[26]M. G. Haines, Can. J. Phys. **64**, 912 (1986).
[27]H. A. Scott and S. B. Hansen, High Energy Density Phys. **6**, 39 (2010).
[28]O. S. Jones, C. J. Cerjan, M. M. Marinak, J. L. Milovich, H. F. Robey, P. T. Springer, L. R. Benedetti, D. L. Bleuel, E. J. Bond, D. K. Bradley *et al.*, Phys. Plasmas **19**, 056315 (2012).
[29]M. Fatenejad, A. R. Bell, A. Benuzzi-Mounaix, R. Crowston, R. P. Drake, N. Flocke, G. Gregori, M. Koenig, C. Krauland, D. Lamb *et al.*, High Energy Density Phys. **9**, 172 (2013).
[30]C. Graziani, P. Tzeferacos, D. Lee, D. Q. Lamb, K. Weide, M. Fatenejad, and J. Miller, Astrophys. J. **802**, 43 (2015).
[31]H. Rinderknecht, M. G. Johnson, A. Zylstra, N. Sinenian, M. Rosenberg, J. Frenje, C. Waugh, C. Li, F. Sèguin, R. Petrasso *et al.*, Rev. Sci. Instrum. **83**, 10D902 (2012).
[32]H. G. Rinderknecht, H. Sio, J. A. Frenje, J. Magoon, A. Agliata, M. Shoup, S. Ayers, C. G. Bailey, M. G. Johnson, A. B. Zylstra *et al.*, Rev. Sci. Instrum. **85**, 11D901 (2014).
[33]B. D. Fried and R. W. Gould, Phys. Fluids **4**, 139 (1961).
[34]M. A. Barrios, D. A. Liedahl, M. B. Schneider, O. Jones, G. V. Brown, S. P. Regan, K. B. Fournier, A. S. Moore, J. S. Ross, O. Landen *et al.*, Phys. Plasmas **23**, 056307 (2016).
[35]C. K. Li, A. B. Zylstra, J. A. Frenje, F. H. Séguin, N. Sinenian, R. D. Petrasso, P. A. Amendt, R. Bionta, S. Friedrich, G. W. Collins *et al.*, New J. Phys. **15**, 025040 (2013).